

# A Method to Replicate the Microstructure of Heart Tissue *In Vitro* Using DTMRI-Based Cell Micropatterning

NIMA BADIE, LISA SATTERWHITE, and NENAD BURSAC

Department of Biomedical Engineering, Duke University, 3000 Science Drive, 136 Hudson Hall, Durham, NC 27708, USA

(Received 26 June 2009; accepted 26 September 2009; published online 6 October 2009)

**Abstract**—A novel cell culture methodology is described in which diffusion tensor magnetic resonance imaging (DTMRI) and cell micropatterning are combined to fabricate cell monolayers that replicate realistic cross-sectional tissue structure. As a proof-of-principle, neonatal rat ventricular myocyte (NRVM) monolayers were cultured to replicate the tissue microstructure of murine ventricular cross-sections. Specifically, DTMRI-measured in-plane cardiac fiber directions were converted into soft-lithography photomasks. Silicone stamps fabricated from the photomasks deposit fibronectin patterns to guide local cellular alignment. Fibronectin patterns consisted of a matrix of  $190 \mu\text{m}^2$  subregions, each comprised of parallel lines 11–20  $\mu\text{m}$ -wide, spaced 2–8.5  $\mu\text{m}$  apart, and angled to match local DTMRI-measured fiber directions. Within 6 days of culture, NRVMs established confluent, electrically coupled monolayers, and for 18  $\mu\text{m}$ -wide, 5  $\mu\text{m}$ -spaced lines, directions of cell alignment in subregions microscopically replicated DTMRI-measurements with a local error of  $7.2 \pm 4.1^\circ$ . By adjusting fibronectin line widths and spacings, cell elongation, gap junctional membrane distribution, and local cellular disarray were altered without changing the dominant directions of cell alignment in individual subregions. Changes in the anisotropy of electrical propagation were assessed by optically mapping membrane potentials. This novel methodology is expected to enable systematic studies of intramural structure–function relationships in both healthy and structurally remodeled hearts.

**Keywords**—Monolayer, Micro-contact printing, Soft lithography, Cardiac cell alignment.

## INTRODUCTION

Traditional monolayers of cultured cells have been widely used as simplified, but well-controlled, *in vitro* model systems to dissect and study specific physiological and pathophysiological phenomena at the cellular and molecular scale. Their main advantages over intact tissue and organ preparations include a

relatively small number of cells studied, precise control over cellular composition, direct access to cells for electrical and optical measurements, and the absence of uncontrollable systemic effects. With direct diffusional access to cells, monolayer cultures also enable well-controlled and spatially uniform cell conditioning and manipulation by drugs and gene vectors. However, despite exhaustive histological characterizations and significant advances in tissue imaging, current cell culture models still fall short in replicating the realistic structure of intact tissues and organs. Consequently, systematic *in vitro* studies of structure–function relationships in healthy and diseased tissues remain limited.

Cardiac tissue is a particularly important example, as the influence of its complex structure in the normal and pathological electromechanical functioning of the heart has been recognized for centuries. Unfortunately, experimental attempts at correlating structure and function in intact cardiac tissues encounter three major obstacles. First, high spatial resolution electrical measurements from the heart are mainly limited to epicardial and endocardial surfaces, while correlations with intramural structure are only indirectly inferred from cross-sectional histology. Secondly, natural regional heterogeneities in electrical properties of cardiac cells exist throughout the heart, limiting the ability to dissect and study the roles of specific structural features in heart function. Lastly, as each heart is electromechanically and structurally unique, each intact tissue preparation lacks reproducibility, thus complicating correlations across multiple samples.

Some of these issues have been overcome *in vitro* using monolayers of neonatal cardiomyocytes. In particular, the functionally homogenized cell source used in cardiac monolayers allows structure-related phenomena to be dissected from the confounding regional variations in electrical function that are naturally present in the heart. Furthermore, techniques involving the precise deposition of extracellular matrix proteins and cells onto tissue culture substrates

Address correspondence to Nenad Bursac, Department of Biomedical Engineering, Duke University, 3000 Science Drive, 136 Hudson Hall, Durham, NC 27708, USA. Electronic mail: nbursac@duke.edu

(i.e. micropatterning) allow the generation of simplified 2D tissue structures with excellent geometric control and reproducibility. Examples of such structures have included branching or non-branching strands,<sup>26,34</sup> abrupt tissue expansions,<sup>12,35</sup> acellular obstacles,<sup>29</sup> and uniformly anisotropic sheets with varying anisotropy ratios.<sup>6</sup> Importantly, the two-dimensional nature enables direct functional measurements that can be correlated with the underlying tissue structure. Therefore, electrical stimulation and optical mapping of action potential and  $\text{Ca}^{2+}$ -transient propagation have been previously used<sup>9–12</sup> to directly correlate micropatterned tissue structure with the associated electrophysiological function while eliminating any interference from propagation in deeper tissue layers, a concern in studies of the intact heart.

The main limitation of current cardiac monolayer cultures, other than their 2D nature, is that they are generally comprised of either randomly aligned cells (isotropic structure)<sup>4,10,20,31</sup> or cells aligned in a single direction (uniformly anisotropic structure).<sup>5,7</sup> In contrast, natural cardiac tissue consists of fibers and sheets that continuously change direction, twisting and turning throughout the heart wall at both micro- and macroscopic spatial scales.<sup>16,18,27</sup> The inability to recreate this realistic tissue structure in cardiac monolayers has prompted us to develop novel techniques to help bridge the gap between current cell culture models and whole heart preparations.

In this study, we describe in detail a combined cell micropatterning and magnetic resonance imaging methodology to create cardiac cell cultures that exhibit anatomically accurate myocardial structure. Our previous studies have involved micropatterned parallel lines of fibronectin to guide the adhesion and alignment of neonatal rat cardiomyocytes in a single direction or in distinct angles across two neighboring regions.<sup>6</sup> With the current approach, the previous micropatterning technique has been extended to locally guide changes in cell alignment over  $\text{cm}^2$ -sized areas in an effort to replicate the spatially complex microarchitecture imaged from the intact heart.

To obtain information about the detailed three-dimensional architecture of the heart, we utilized diffusion tensor magnetic resonance imaging (DTMRI). DTMRI has been validated as a non-invasive technique to measure 3D fiber directions of the healthy and diseased heart and brain with high spatial resolution.<sup>17,19,37,38</sup> As a proof-of-principle, DTMRI-measured fiber directions of a transverse murine ventricular cross-section were replicated in 2D micropatterned cardiac monolayer cultures with high accuracy and reproducibility. In addition, local cellular disarray and the presence of fibroblasts were each systematically varied while maintaining realistic

cellular alignment. The described methodology represents a novel paradigm in cardiac cell culture which we believe will enable unique insights into the roles of realistic intramural tissue structure and cellular composition in normal and disease-related cardiac conduction and arrhythmias.

## MATERIALS AND METHODS

### *Photomask Design*

For this study, DTMRI data from a mouse ventricle was kindly provided by our colleagues.<sup>21</sup> Example datasets from other species, as well as diseased hearts, are publicly available at <http://www.ccbm.jhu.edu>, while additional datasets are constantly being generated. Starting from a DTMRI dataset of interest, six 3D arrays were loaded into MATLAB (The Mathworks), three of which were primary eigenvector components ( $u$ ,  $v$ ,  $w$ ) describing the local 3D direction of cardiac fibers, and another three were spatial components ( $x$ ,  $y$ ,  $z$ ) describing the corresponding coordinates in the heart. For a heart cross-section of interest, the intersecting vectors were projected onto the cross-sectional plane to yield an array of 2D in-plane fiber direction vectors. In-plane angles ( $\theta$ , from  $-90^\circ$  to  $+90^\circ$ ) were assigned to each vector to yield a 2D angle map, shown as quivers in Figs. 1a and 1b (e.g. for projection onto a transverse ( $z$ ) cross-section, the  $u$  and  $v$  vector components at that plane were simply extracted and assigned an in-plane angle of  $\theta = \tan^{-1}(v/u)$ ).

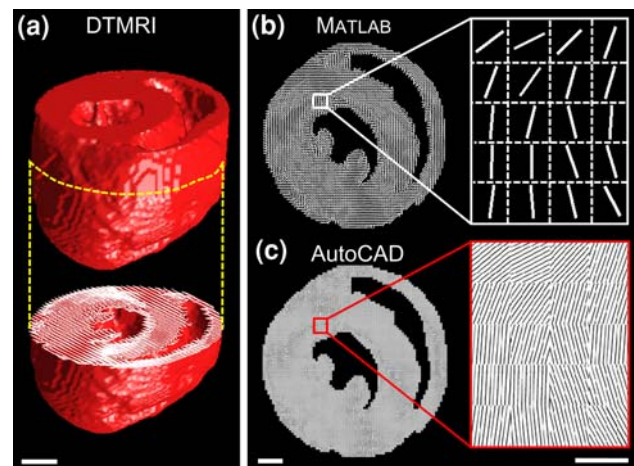


**FIGURE 1. Design of micropatterning photomask. (a)** Transverse cross-section from murine ventricle with overlaid in-plane DTMRI fiber direction quivers. **(b)** Projected fiber direction map calculated in MATLAB. **(c)** Corresponding AutoCAD micropattern, where the DTMRI angle map was converted to a pixelated array of angled parallel lines. White regions correspond to fibronectin-printed areas on the coverslip. Scalebars: (a) 1 mm; (b–c) 2 mm left side, 250  $\mu\text{m}$  right side.

The photomask pattern was drawn in AutoCAD (Autodesk). The function *fprintf* in MATLAB was used to write three AutoCAD-compatible \*.LSP files: two position files ( $x$  and  $y$ ) and one corresponding angle file ( $\theta$ ), all in vector form. In order to load vectors into AutoCAD, \*.LSP files were created in the following format, where  $x = [x_1 \ x_2 \ \dots \ x_i \ \dots]$ :

```
(setq x (list (cons 1 x1)
              (cons 2 x2) ...
              (cons i xi) ...))
```

Using the AutoLISP programming language, the  $x$ ,  $y$ , and  $\theta$  \*.LSP files were loaded into AutoCAD. For example, for the vector  $x$ , commands used were:

```
(load "x_file.lsp")
(setq x1 (cdr (assoc 1 x))
      x2 (cdr (assoc 2 x)) ...
      xi (cdr (assoc i x) ...))
```

For each element of the DTMRI-derived 2D angle map, the AutoLISP programming language was used to draw a square "pixel" subregion ( $190 \times 190 \mu\text{m}^2$  used here) centered at  $(x_i, y_i)$  consisting of angled

parallel lines ( $18 \mu\text{m}$  wide, spaced  $5 \mu\text{m}$  apart used here) aligned to the corresponding angle ( $\theta_i$ ), as shown in Fig. 1c. A square border (1 mm thick) was drawn around the entire cross-section micropattern, 2 mm away from all features. This border ultimately limited stamp sagging and undesired cell adhesion outside of patterned areas. The micropattern was finally printed as a high resolution glass photomask (chrome on soda-lime, Advance Reproductions Inc.).

### Soft Lithography and Micro-Contact Printing

The details of the microfabrication procedure are shown in Fig. 2. A virgin 4-in. silicon wafer (WaferWorld) was first "piranha-etched" in a solution of 1 part  $\text{H}_2\text{O}_2$ , 3 parts  $\text{H}_2\text{SO}_4$  at  $80^\circ\text{C}$  for 10 min, then thoroughly rinsed in fresh deionized water. The wafer was transferred to a  $200^\circ\text{C}$  hotplate (720 Series, PMC) for 5 min for surface dehydration, cleaned with a  $\text{N}_2$  gun, and UV-decontaminated (UV decontamination system, Novascan PSD-UVT, Novascan Technologies) for 8 min. Negative photoresist (SU8-2, Microchem Inc.) was spin-coated onto the wafer at 1000 rpm for 1 min (programmable spin-coater, Headway Research,

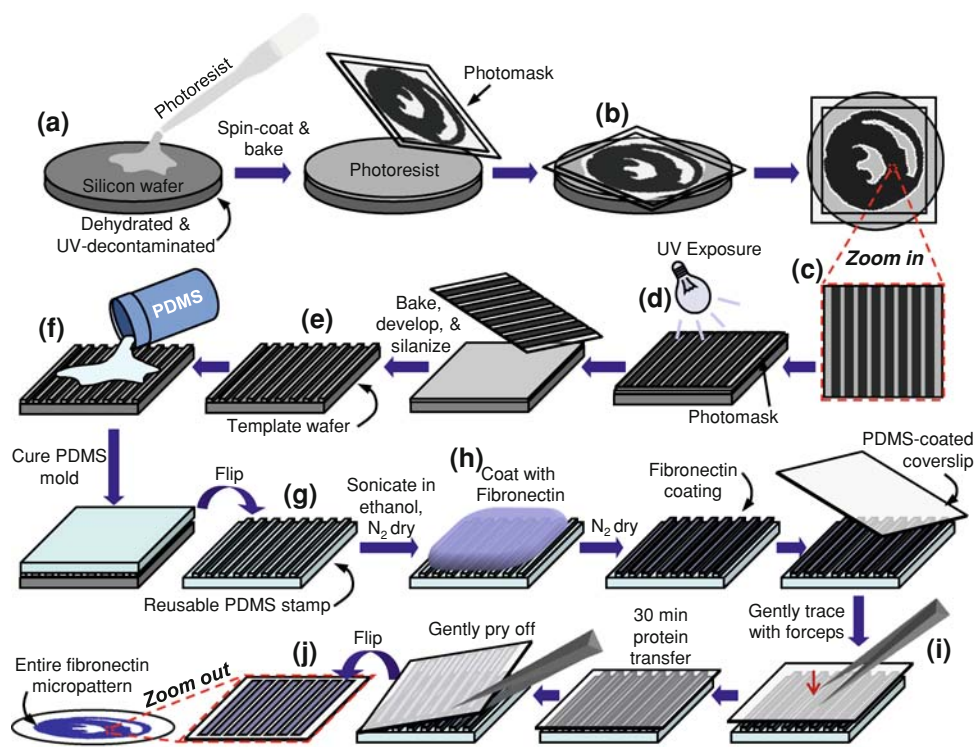


**FIGURE 2.** Schematic of the photolithography and microcontact printing methodology. (a) Photoresist was spin-coated and baked onto a UV-decontaminated silicon wafer and (b) covered with the photomask. (c) Close-up of one pixel parallel-line pattern is shown for simplicity. (d) The photoresist was exposed to UV light through the photomask, baked, developed, and silanized to yield a template wafer (e). PDMS (shown in light blue) was poured on the template wafer (f) and cast as a reusable stamp (g), which was cleaned and coated with fibronectin (shown in purple, h). Fibronectin was dried by  $\text{N}_2$  gas, and a PDMS-coated coverslip was lightly pressed down on the stamp with forceps (i) for protein transfer and eventually pried off to reveal a fibronectin-micropatterned coverslip (j). *Note:* elements not drawn to scale.

PW3200730-D) to obtain a 5  $\mu\text{m}$  thick layer. The spin-coated wafer was baked on the hotplate at 65 °C for 1 min followed by 95 °C for 3 min. The wafer with baked photoresist was then exposed to a collimated 350 W UV light for 15 s through the photomask using a mask aligner (SUSS MicroTec MA/BA6 Mask Aligner) under “hard contact” mode. The exposed wafer was returned to the hotplate and baked again at 65 °C for 1 min and 95 °C for 3 min. The temperature was ramped down to 25 °C at 8 °C/h to reduce stress to the photoresist-silicon bond. Finally, the photoresist was developed in PGMEA (propylene glycol methyl ether acetate, Aldrich) for 2 min and rinsed with isopropyl alcohol. After rinsing, the developed wafer was  $\text{N}_2$ -dried and visually assessed under a metallurgic microscope (VWR VistaVision) to ensure uniform line widths and spacings, the absence of dust or other impurities, and no photoresist detachment. The microfabricated *template wafer* was then left overnight at room temperature inside a vacuum desiccator containing a micro slide with 1 drop of silane solution ((tridecafluoro-1,1,2,2-tetrahydro octyl)-1-trichlorosilane, UCT Specialties), to render the wafer surface “non-stick”.

To create complementary PDMS (poly-dimethylsiloxane, Sylgard 184, Dow Corning) stamps, 20 g elastomer base and 2.0 g curing agent were thoroughly mixed and then de-gassed in a vacuum desiccator for 20 min. The mixture was poured directly onto the silanated template wafer in a 100 mm diameter Petri dish and baked in an 80 °C oven (Isotemp Vacuum Oven, Model 280A, Fisher Scientific) for 2 h to cure the PDMS. The cured PDMS was then peeled from the wafer and cut with a razor blade into individual, reusable stamps. Meanwhile, 5 g elastomer base was thoroughly mixed with 0.5 g curing agent to PDMS-coat 22 mm glass coverslips (No. 1, VWR). Approximately 250  $\mu\text{L}$  was spin-coated onto each coverslip at 4000 rpm for 20 s. Coverslips were transferred by hand to a Petri dish, avoiding contact with the PDMS-coated surface, and baked in an 80 °C oven for 1 h.

Before each use, the stamps were sonicated in 70% ethanol for 20 min (Branson 1510, Branson Ultrasonic Corp.), dried with a  $\text{N}_2$  gun, and placed, feature-side up, onto a Petri dish in a sterile hood. Using a sterile pipette tip, each stamp was evenly coated with 400  $\mu\text{L}$  fibronectin solution (50  $\mu\text{g}/\text{mL}$  dissolved in  $\text{H}_2\text{O}$ , human fibronectin, BD). The coated stamps were placed in a tissue culture incubator (IR Autoflow, NUAIRE) for 1 h. At the end of the stamp incubation, the PDMS-coated coverslips were UV-decontaminated for 8 min. In a sterile hood, the fibronectin-coated stamps were dried with the  $\text{N}_2$  gun. Using fine forceps, each coverslip was then gently placed, PDMS-side-down, onto a dried stamp. One tip of the fine forceps was then gently traced across the back of the coverslip

along the features of the underlying stamp to ensure contact. After 30 min, the coverslip was slowly pried from the stamp. Each coverslip was finally transferred, fibronectin-side-up, into the well of a 12-well plate (Linbro) containing 2 mL PBS (Gibco). Patterned coverslips were stored in the sterile hood at room temperature until ready for cell seeding (up to 4 h).

### Cell Culture

Ventricular cells were enzymatically isolated from 2 day old neonatal Sprague–Dawley rats as previously described.<sup>24,32</sup> The standard, highly cardiomyocyte-enriched cell suspension was obtained after two preplating steps, during which the faster-attaching non-cardiomyocytes (i.e., fibroblasts<sup>30,32</sup>) were discarded. The cells were diluted in our standard *cell seeding medium* (M199 (Gibco) supplemented with 10% (v/v) fetal calf serum (Hyclone), 10% (v/v) horse serum (Hyclone), 1% (v/v) HEPES (100x, Gibco), 1% (v/v) MEM non-essential amino acids (Gibco), 1% (v/v) GlutaMAX (Gibco), glucose (4 mg/mL, Sigma), vitamin B<sub>12</sub> (2  $\mu\text{g}/\text{mL}$ , Sigma), and penicillin-G (20 U/mL, Sigma)) to a concentration of 250,000 cells/mL. Two milliliters of the cell suspension was added to each well of the 12-well plate, which was stored in an incubator at 37 °C for 4 h to allow cell adhesion. Coverslips were then rinsed with PBS and returned to the incubator in fresh *cell seeding medium*. The *cell seeding medium* was replaced with *cell maintenance medium* after 24 h and every other day thereafter. *Cell maintenance medium* was identical to *cell seeding medium*, but with 2% (v/v) fetal bovine serum (Gibco) replacing the fetal calf and horse sera.

### Immunofluorescence

One, three, and six days after cell seeding, the coverslips were harvested and immunostained as previously described.<sup>32</sup> Briefly, cultures were fixed, permeabilized, blocked, and incubated with primary antibodies for 1 h (anti-sarcomeric  $\alpha$ -actinin, anti-connexin43, anti-vimentin, Sigma) followed by secondary antibodies (Molecular Probes) and/or stains (DAPI, Phalloidin-FITC, Sigma) for 1 h. Sarcomeric  $\alpha$ -actinin, connexin43, and nuclear stains were used for qualitative structural analysis, phalloidin-FITC alone was used for quantitative angle alignment analysis, and phalloidin-FITC in conjunction with vimentin was used for the assessment of cellular composition.

### Image Acquisition

Image acquisition was performed using a fluorescence microscope (Nikon, Eclipse TE2000-U) equipped

with a 10× objective (Nikon), a high-resolution CCD camera (SensiCam QE, Cooke Corp., 1376 × 1040 pixels, 6.45 × 6.45 μm<sup>2</sup>/pixel), and an automated XYZ stage (Prior Proscan). The prepared slide was manually rotated and secured onto the stage such that the *XY* motion of the stage was aligned with the rows/columns of the pattern's square subregions (Fig. 5a). Using Metamorph (Molecular Devices), a “journal” (i.e. macro) was created that executes the following tasks, in order: auto-focus, auto-expose, acquire image, save image (recording the acquisition number in the file-name), and close image window. Using the joystick, the stage was translated to the top edge of the culture to record the *y*-position, “*y*<sub>0</sub>,” and then to the left edge to record the *x*-position, “*x*<sub>0</sub>.” The stage was then translated to (*x*<sub>0</sub>, *y*<sub>0</sub>) to the field-of-view corresponding to the top-left corner of the entire culture (Fig. 5a).

The *scan stage* function was used in conjunction with the previously saved “journal” to acquire an array of images encompassing the entire culture. The scan stage step size was calculated based on the number of subregions in each image and the size of each subregion. The number of rows and columns of images that must be acquired to capture all subregions in the culture was calculated based on the field-of-view and total culture size. The result was a set of grayscale image files in a single directory, where a small array of micropatterned subregions was captured by each image.

#### Analysis of Cell Alignment

Image processing was performed in MATLAB to calculate the local angles of cell alignment throughout the patterned cell culture. Each of the acquired images was loaded into MATLAB and subdivided into image subregions, corresponding to the 190 × 190 μm<sup>2</sup> micropatterned cell culture subregions. For each image subregion, “*A*” (consisting of a 2D matrix of image pixels with dimensions that depend on the camera resolution and image magnification), the dominant angle of cell alignment was calculated as outlined in Fig. 5c, and described elsewhere.<sup>22</sup> Briefly, the following horizontal (*S*<sub>*x*</sub>) and vertical (*S*<sub>*y*</sub>) Sobel edge-detection filters (5 × 5 matrices) were constructed:

$$S_x(i, j) = j \cdot e^{-(i^2+j^2)/2}, \quad S_y(i, j) = i \cdot e^{-(i^2+j^2)/2}$$

for  $i = [-2, 2]$  and  $j = [-2, 2]$ .

Next, each edge-detection filter was convolved with image subregion “*A*”, to calculate the *x*- and *y*-direction edge intensities,  $E_x = S_x \otimes A$  and  $E_y = S_y \otimes A$ ,

respectively. For all image pixels, the local angles of cell alignment,  $\Phi$ , were calculated as:

$$\Phi = \tan^{-1}(-E_y/E_x) + \frac{\pi}{2} \in \left[-\frac{\pi}{2}, \frac{\pi}{2}\right]$$

The dominant angle of cell alignment in each subregion ( $\Phi^{\text{dom}} \in [-\frac{\pi}{2}, \frac{\pi}{2}]$ ) was determined by taking the cumulative angular sum of all of its pixel angles. If the average grayscale image intensity value of subregion “*A*” was below 10% of the maximum subregion value in the culture, the subregion “*A*” was defined as acellular and assigned a dominant angle of cell alignment of NaN (not a number).

Each dominant subregion angle was assigned to its appropriate coordinate in the cell culture cross-section to construct a composite 2D *cell culture angle map*. The resulting *cell culture angle map* could then be directly compared to the original *DTMRI angle map* on which it was based. The absolute *angle difference*,  $\Delta\Phi$ , was calculated between each value in the *cell culture angle map*,  $\Phi^{\text{culture}}$ , and the corresponding value in the *DTMRI angle map*,  $\Phi^{\text{DTMRI}}$  as follows:

$$\Delta\Phi_{ij} = \left| \Phi_{ij}^{\text{culture}} - \Phi_{ij}^{\text{DTMRI}} \right|,$$

$$\Delta\Phi_{ij} = \begin{cases} \Delta\Phi_{ij} & \text{if } \Delta\Phi_{ij} \leq 90 \\ 180 - \Delta\Phi_{ij} & \text{if } \Delta\Phi_{ij} > 90, \end{cases} \quad \Delta\Phi_{ij} \in (0, 90).$$

#### Analysis of Local Structural Anisotropy

The influences of fibronectin line width and spacing on structural anisotropy in patterned monolayers were quantified on a cell-by-cell basis. Specifically, individual cells in fluorescence images with immunostained sarcomeric  $\alpha$ -actinin and connexin43 were manually traced using Photoshop (CS3 Extended, Adobe Systems, Inc.) and analyzed in MATLAB. Each traced cell boundary was used to find the best-fit ellipse, and determine its major and minor axes. Major-to-minor axis ratio, approximating cell length-to-width ratio (“elongation ratio”), was used to quantify cell elongation. Gap junctions (i.e. connexin43-labeled pixels that exhibit intensities greater than 30% of the full range and existed within 3.5 μm from the traced cell boundary) were classified as “side-to-side” if they were within a radius ( $r = 0.9 \times$  half-major axis) from the center of the ellipse, and classified as “end-to-end” otherwise. For each cell, end-to-end and side-to-side gap junction membrane density was obtained by dividing the number of end-to-end and side-to-side gap junction pixels with “end” and “side” arc lengths of the cell's fitted ellipse, respectively. The end-to-side distribution of gap junctions was quantified by calculating the ratio of the “end-to-end” to “side-to-side” gap junction membrane densities. The local

cellular “disarray” within each  $190 \times 190 \mu\text{m}^2$  subregion was quantified as the mean deviation of each cell’s orientation (being along the major axis of the fitted ellipse) from the dominant cell orientation for that subregion.

### Optical Mapping of Membrane Potentials

Optical mapping recordings of action potential propagation during 2 Hz stimulation were performed as previously described.<sup>3</sup> Briefly, coverslips were stained with a voltage sensitive dye (Di-4 ANEPPS,  $16 \mu\text{mol/L}$ ) for 5 min, transferred to a custom, thermo-regulated chamber perfused with Tyrodes solution, and stimulated with a platinum bipolar point electrode. Optical signals were recorded by a 504 optical-fiber photodiode array (RedShirt Imaging). Action potential activation times, defined as the times of maximum upstroke, were registered onto the culture’s corresponding DTMRI angle map to produce isochrone maps of activation.<sup>3</sup> Local conduction velocities were calculated from activation times and spatially averaged across the entire mapping area as previously described.<sup>3</sup>

### Statistical Analysis

All values were reported as mean  $\pm$  SD with the statistical significance analyzed using one-way ANOVA followed by post hoc Tukey’s multiple comparison tests. Angle differences between corresponding subregions in different anisotropy settings and the original DTMRI angles were compared using a paired Student’s *t*-test. Differences were considered statistically significant for  $p < 0.05$ .

## RESULTS

Using the described microfabrication methods, the in-plane DTMRI fiber directions were translated into a photomask containing an array of subregions composed of angled parallel lines. A photomask with  $20 \mu\text{m}$ -wide lines spaced  $3 \mu\text{m}$  apart ultimately yielded a template wafer with features  $5.3 \mu\text{m}$  tall,  $5 \mu\text{m}$  wide, and spaced  $18 \mu\text{m}$  apart (Fig. 3a). The widening of the features relative to initial photomask pattern (e.g., from a  $3 \mu\text{m}$  spacing to a  $5 \mu\text{m}$  wide ridge) was a result of UV light diffraction. The PDMS stamp cast as a negative replica of these microfabricated features served to deposit an array of  $190 \mu\text{m}$ -sized square subregions containing  $18 \mu\text{m}$ -wide fibronectin lines spaced  $5 \mu\text{m}$  apart (Fig. 3b). The width and spacing of fibronectin lines were also varied using various photomask patterns while maintaining the subregion size of  $190 \mu\text{m}$ . In particular, for the patterns in Figs. 3b–3d, the width of the lines was varied from 11 to  $18 \mu\text{m}$  while their spacing was varied from  $2.0$  to  $8.5 \mu\text{m}$ .

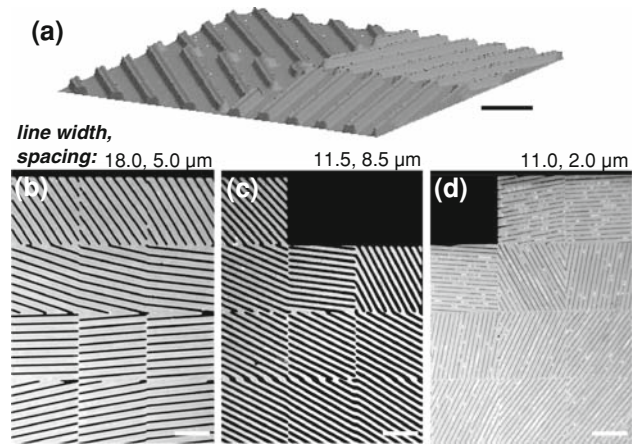


**FIGURE 3.** Template wafer and microcontact-printed fibronectin. (a) Representative optical profile of four subregions from the microfabricated template wafer. Fabricated features were  $5.33 \mu\text{m}$  tall. Wafers with different feature width and spacing were used to create different fibronectin micropatterns. (b–d) Microcontact-printed fluorescent fibronectin lines (light) of various widths and spacings (dark), fabricated from different template wafers. Scalebars: (a)  $50 \mu\text{m}$ ; (b–d)  $100 \mu\text{m}$ .

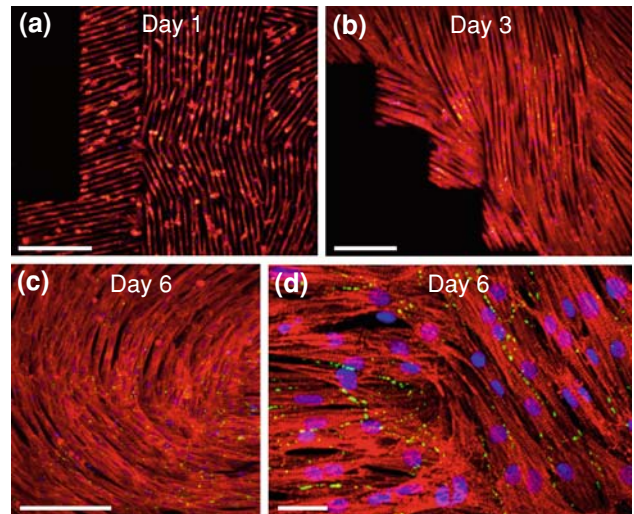


**FIGURE 4.** Formation of realistic cell alignments in micropatterned cultures. After seeded cells adhered at day 0 (a), they spread and aligned along the underlying fibronectin lines (shown for  $18 \mu\text{m}$  width,  $5 \mu\text{m}$  spacing) (b), and formed confluent cardiac fibers by day 6 (c). Cardiac fibers transitioned across different pixel borders in a continuous fashion. (d) A close-up near two pixels at day 6 shows the presence of aligned, cross-striated cardiomyocytes interconnected via connexin-43 gap junctions. Red: sarcomeric  $\alpha$ -actinin, green: connexin-43, blue: nuclei. Scalebars: (a–c)  $250 \mu\text{m}$ ; (d)  $50 \mu\text{m}$ .

Similar to our previous studies of macroscopic cell alignment,<sup>6</sup> fibronectin lines enabled cell adhesion and spreading while the unpatterned areas of the PDMS-coated coverslip remained acellular. The seeded cells began to spread and elongate along fibronectin lines (for all line widths and spacings) by culture day 1 (Fig. 4a), crossed to neighboring lines by day 3

(Fig. 4b), and ultimately formed a confluent monolayer by day 6 (Figs. 4c and 4d). Cardiomyocytes formed fibers that exhibited clear cross-striations and abundant intercellular coupling (as assessed by sarcomeric  $\alpha$ -actinin and connexin43 stainings, respectively, Fig. 4d). Once cell confluence was established, the bulk of cells in the centers of individual subregions aligned along their underlying fibronectin lines. The cells at the subregion periphery smoothly transitioned to neighboring subregions (Fig. 4c), thus maintaining confluence even for sharp turns in fiber direction (Fig. 4d).

To quantify directions of cell alignment in individual subregions, immunofluorescence images were systematically acquired by scanning the entire micropatterned cell culture area. The calculated directions of cell alignment in all subregions were used to assemble a

cell culture angle map with one-to-one correspondence with the original DTMRI map. As a result, we were able to directly quantify the local agreement between the natural, DTMRI-measured in-plane myofiber directions and those of the micropatterned cultures. For the cross-section shown in Fig. 5a ( $18\ \mu\text{m}$  wide,  $5\ \mu\text{m}$  spaced lines), dominant angles of cell alignment in over 4000 cellular subregions (within the  $15.2 \times 13.3\ \text{mm}^2$  culture area) exhibited a mean absolute angle difference of  $7.2 \pm 4.1^\circ$  (mean  $\pm$  SD among all subregions) compared to the original DTMRI pattern (Fig. 5d). Similar average angle differences have been measured when validating the accuracy of DTMRI against corresponding histological sections in the same heart<sup>17,19</sup> and between anatomically registered DTMRI-measurements among multiple hearts.<sup>16</sup>

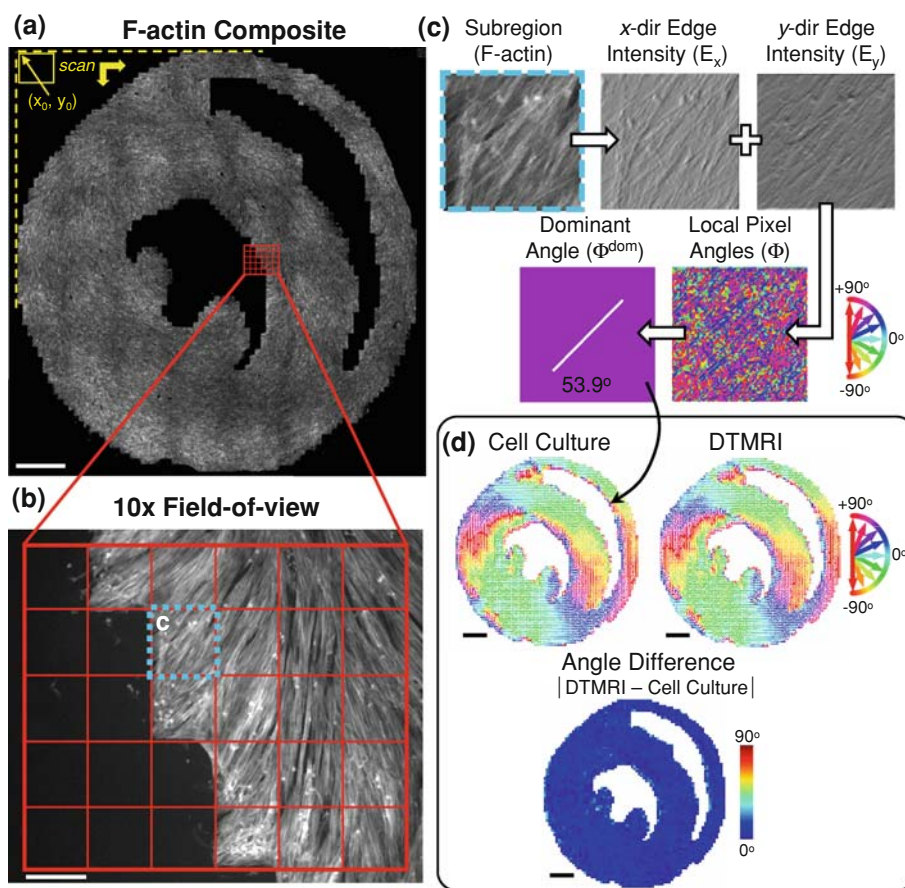


**FIGURE 5.** Assessment of cell alignment in micropatterned cross-sections. (a) Composite F-actin image of the entire cross-section produced using the photomask from Fig. 1. Yellow field-of-view shown at the origin (image at upper-left:  $x_0, y_0$ ) was used for automated left-to-right, top-to-bottom scanning. (b) Sample field-of-view obtained using  $10\times$  objective. Red grid subdivides the image into a  $5 \times 6$  array of subregions. (c) Calculation of dominant fiber angle in sample subregion from (b), outlined in light blue. Calculated  $x$ - and  $y$ -direction edge intensities were used to calculate the local image-pixel angles, which were then averaged to obtain the subregion's dominant fiber angle (see text for additional details). (d) Validation of local cell alignment in patterned cross-section. Dominant fiber angles calculated for each subregion were compiled into a *cell culture angle map* and directly compared (for all 4000 subregions) to the original *DTMRI angle map*. The resulting *angle difference map* exhibits a mean angle difference of  $7.2^\circ$ , demonstrating the accuracy in translating DTMRI-measured realistic cardiac microstructure into a micropatterned cell culture. Scalebars: (a) 2 mm; (b)  $190\ \mu\text{m}$ ; (d) 2 mm.

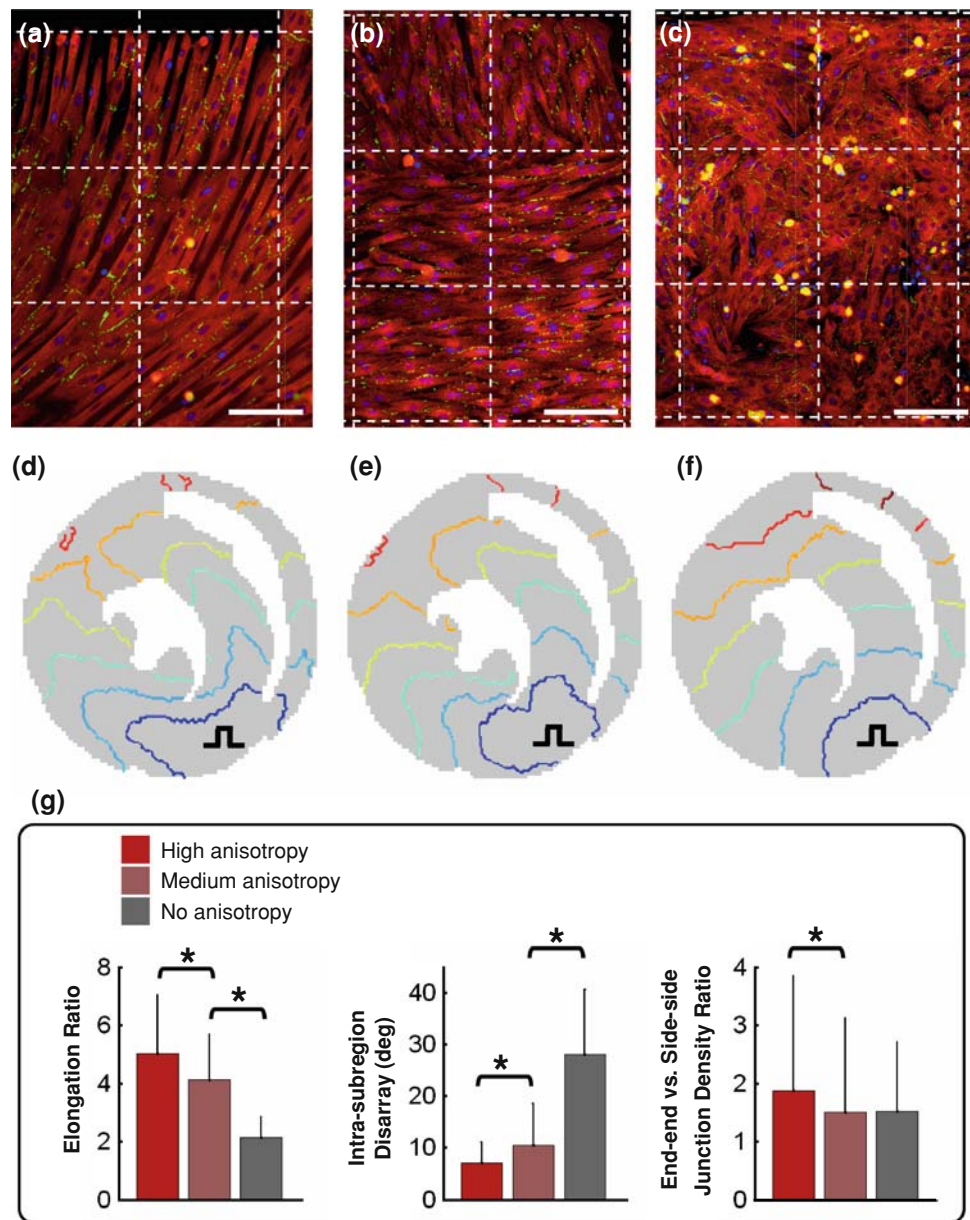


**FIGURE 6.** Control of structural and functional anisotropy ratio. Micropatterned cross-sections were produced with varying degrees of local structural anisotropy using fibronectin line widths and spacings of (a) 18 and 5  $\mu\text{m}$ , (b) 20 and 3  $\mu\text{m}$ , or (c) solid patterns with no lines. *Red*: sarcomeric  $\alpha$ -actinin, *green*: connexin-43, *blue*: nuclei. (d–f) Isochrone maps of the resulting propagation initiated by a point electrode placed at the same locations (pulse symbol) relative to tissue boundaries. Colored isochrone lines denote wavefronts with activation times spaced every 8 ms. Note the progressive decrease in the degree of local functional anisotropy (i.e. change from elliptical to circular propagation patterns) in (d–e) dictated by the apparent decrease in structural anisotropy. (g) This apparent decrease in structural anisotropy was associated with a reduction in cellular elongation (length:width ratio,  $p < 0.001$ ), an increase in local cellular disarray (mean angle deviation from the subregion's dominant cell orientation,  $p < 0.05$ ), and a reduction in the end:side ratio of gap junction membrane density from the highest anisotropy setting (connexin-43 positive fraction of cell membrane, end:side,  $p < 0.05$ ). High, medium, and no anisotropy bars correspond to culture settings with example images shown in (a–c), respectively.  $N > 250$  cells/group, 2 cultures/group. Scalebars: (a–c) 100  $\mu\text{m}$ .

The described micropatterning techniques not only provide precise control over the dominant direction of local cell alignment within individual subregions, but can also provide control over the degree of local structural anisotropy (e.g., cell elongation, degree of cell disarray, etc.) by adjusting the line widths and

spacings of the micropattern. For instance, 18  $\mu\text{m}$ -wide lines with 5  $\mu\text{m}$  spacings (Fig. 6a) produced more elongated and aligned cells than 20  $\mu\text{m}$ -wide lines and 3  $\mu\text{m}$  spacings (Fig. 6b). In contrast, isotropic patterns with solid, rather than lined, subregions produced the same gross anatomical boundaries of the ventricular



cross-section, but exhibited more polymorphic cell shapes and random, rather than realistic, cell alignment (Fig. 6c). The influence of the degree of structural anisotropy on electrical conduction was assessed using voltage-sensitive dyes and optical mapping of action potential propagation. As activation isochrone maps (Figs. 6d–6f) illustrate, a higher degree of structural anisotropy resulted in more lobed, elliptical propagation patterns, indicating a higher degree of local functional anisotropy. Meanwhile, the spatially averaged conduction velocities in the three settings were similar (mean  $20.4 \pm 2.1$  cm/s) and comparable with those previously reported for anisotropic neonatal rat cardiac monolayers.<sup>3,6,41</sup>

To determine the specific structural characteristics that yielded the observed changes in local functional anisotropy for these three culture settings (Figs. 6d–6f), we quantified the degree of cell elongation, distribution of gap junction density along the cell membrane, and local cellular disarray within each subregion. As shown in Fig. 6g, by controlling fibronectin line width and spacing, local functional anisotropy was increased by increasing cellular elongation (increased cell length:width ratio from  $2.14 \pm 0.71$  in isotropic cultures to  $4.13 \pm 1.57$  and  $5.02 \pm 2.02$  in anisotropic cultures,  $p < 0.001$ ) and decreasing cellular disarray (decreased difference from subregion's dominant fiber direction from  $28.1 \pm 12.5^\circ$  in isotropic cultures to  $10.5 \pm 8.0^\circ$  and  $7.1 \pm 4.1^\circ$  in anisotropic cultures,  $p < 0.005$ ). Despite differences in cell elongation and disarray, the dominant direction of cell alignment within each subregion was consistent in the two anisotropic settings (mean difference between each of the two settings and the corresponding DTMRI angles of  $9.1 \pm 0.9^\circ$ ,  $p = 0.3$ ). Meanwhile, the gap junction membrane density at cell ends relative to cell sides was slightly increased only in the highest anisotropy setting ( $1.52 \pm 1.19$ ,  $1.51 \pm 1.61$ ,  $1.87 \pm 1.98$ , Fig. 6g).

In addition to tissue microstructure, the described methodology can enable independent control over cellular composition. As an example (see Supplemental Material), we prepared neonatal rat cardiac cells with different fractions of cardiomyocytes and fibroblasts by simply employing a different number of preplating steps during the cell dissociation procedure. By applying this methodology, cardiac tissue microstructure was relatively preserved, while the “fibrotic” area could be independently varied.

## DISCUSSION

This paper details and validates a novel cell culture methodology in which DTMRI-measured cardiac fiber

directions were combined with high-resolution cell micropatterning to yield realistic *in vitro* replicas of mouse ventricular cross-sections. Our previous culture techniques used parallel lines of fibronectin to establish unidirectional cardiac cell alignment over  $\text{cm}^2$ -sized areas.<sup>6</sup> This macroscopic approach has been scaled down in the current methodology to locally guide cell orientation within each of the several thousand microscopic subregions, forming a confluent, relatively large cardiac monolayer culture. As such, this high resolution micropatterning technique enables the design of any desired 2D pattern of cardiac fiber directions in cell culture.

In this particular approach, the entire cell culture substrate was discretized into a 2D array of  $190 \mu\text{m}^2$  subregions containing parallel fibronectin lines angled to match the discrete data points of the DTMRI matrix. Within each subregion, cultured cardiomyocytes adhered and aligned along the underlying lines and ultimately transitioned between lines and across subregions (Fig. 4) to establish a confluent, well-spread, and well-coupled anisotropic monolayer with realistic tissue boundaries (Fig. 5a). Immunofluorescence and custom cell angle analysis revealed the realistic DTMRI-measured cardiac fiber directions to be accurately replicated in cell culture on a microscopic scale (Fig. 5d).

Despite discrete changes in the direction of underlying fibronectin lines, cultured neonatal cardiomyocytes demonstrated the intrinsic ability to create continuous fibers that smoothly transitioned between neighboring subregions. Differences between directions of local cell alignment and the original DTMRI directions, although small, were largest in the regions where fibronectin lines sharply changed orientation between neighboring subregions (not shown). While more complex approaches to design continuous fibronectin lines throughout the entire culture (e.g. fiber tractography<sup>33</sup>) are expected to yield even better agreement between local cell orientation and DTMRI data, we feel that the described approach provides sufficient accuracy, indeed comparable to that of the DTMRI method itself.<sup>17,19</sup>

Importantly, because the cellular micropatterns are based on DTMRI data of the entire heart, any full-length tissue cross-section can be replicated and electrophysiologically studied, as opposed to only a portion of exposed surface in studies of intact hearts. There is virtually no limit to the heart cross-section size that can be micropatterned, as standard photolithographic equipment can accommodate  $5 \times 5 \text{ in.}^2$  photomasks, thus allowing the reproduction of cross-sections from hearts of various sizes and species, including human. We have previously shown that neonatal cardiomyocytes in culture can undergo

a sharp change in direction over distances as short as 50–100  $\mu\text{m}$ .<sup>3,6</sup> As the current resolution of DTMRI varies between  $\sim 70 \mu\text{m}$  and  $\sim 2 \text{ mm}$  (depending on the size of the heart and strength of the imaging magnet),<sup>14,19,21,36,37,42</sup> highly accurate agreement between cell orientation in culture and that measured by DTMRI can be readily achieved for a variety of conditions.

Furthermore, for given directions of local cell alignment, we showed that the degree of local structural anisotropy could be varied by tuning the photo-mask design to control the width and spacing of the patterned fibronectin lines. In particular, quantitative immunostaining demonstrated that altered dimensions (but not directions) of fibronectin lines yielded the expected changes in the degree of cell elongation and local cellular disarray (Fig. 6g) with negligible differences in the dominant direction of cell alignment in individual subregions. Meanwhile, the end-to-end relative to side-to-side gap junctions per unit length were greater in only the highest anisotropy setting. The increased structural anisotropy corresponded to an increased degree of functional anisotropy, as assessed by optically mapping action potential propagation (Figs. 6d–6f). Meanwhile, the average conduction velocity in different culture settings was unchanged. Thus, changes in electrical anisotropy in these culture settings were dominated by changes in cell geometry and local disarray, with a contribution by the gap junction membrane distribution in only the highest anisotropy setting.

The demonstrated ability to locally (or globally) alter anisotropy *in vitro* while maintaining realistic fiber directions is important because the degree of natural cardiac tissue anisotropy changes with the stage of the postnatal development, region of the heart,<sup>41</sup> aging,<sup>25,40</sup> and cardiac disease.<sup>8</sup> Thus, with simple adjustments of the fibronectin micropattern, the described cell culture approach allows unique studies of the individual and combined roles of (1) realistic tissue boundaries, (2) local fiber directions, and (3) local structural anisotropy (cell elongation, disarray) in cardiac electrical conduction, and all independent of spatial gradients in ion channel expression naturally present in the heart. Using this and similar approaches to identify intramural sites with potentially arrhythmogenic tissue structure could eventually lead to improved targets for cardiac pacing or ablation.

Although the outlined approach uses neonatal rat cardiomyocytes, the same procedure could be extended to other cell types. With respect to cardiac disease and cell therapy in particular, the interactions between cardiomyocytes and non-myocytes (e.g. fibroblasts, different types of stem cells) could be studied in micropatterned co-cultures that mimic both the realistic

cardiac tissue structure derived by DTMRI and the cellular composition obtained from immunohistological sections. As a simple example, the cellular composition in monolayers with realistic tissue structure was varied in this study by co-culturing distinct ratios of cardiomyocytes and fibroblasts (Supplemental Fig. 1). If media supplements (e.g. TGF- $\beta$ , ascorbic acid, angiotensin II<sup>13,15,28</sup>) were also used to increase the fibroblast secretion of collagen I, the resulting culture setting would capture several characteristics of fibrotic heart tissues.<sup>23,39</sup> These and other modifications of basic culture conditions (representing healthy heart tissue) could be used in the future to systematically study the roles of remodeled tissue structure and cell composition in pathological cardiac conduction. Importantly, since DTMRI can be performed non-invasively *in vivo*,<sup>42</sup> disease-related structural remodeling can be tracked in the same subject over time. In these cases, studies of realistic micropatterned cultures from different stages of disease could help elucidate the roles of progressive structural remodeling in the development of electrophysiological dysfunction.

As with all model systems, this approach is not without its limitations, the most obvious being its two-dimensional nature, which can provide insight into only in-plane patterns of electrical propagation. Although the spatiotemporal dynamics of cardiac tissue naturally occur in three dimensions, specific cross-sections with minimal out-of-plane fiber angles<sup>3</sup> can be used to study realistic patterns of propagation that may develop inside the intact tissue when stimulated from an in-plane site. In general, using this novel model system, the complex roles of healthy or remodeled cardiac microarchitecture in macroscopic impulse conduction and reentrant arrhythmias can be studied for the first time in a systematic and reproducible fashion.<sup>1,2</sup> In order to facilitate the transfer of this versatile methodology to interested research groups, we also present troubleshooting tips in the Supplemental Material.

## ELECTRONIC SUPPLEMENTARY MATERIAL

The online version of this article (doi:[10.1007/s10439-009-9815-x](https://doi.org/10.1007/s10439-009-9815-x)) contains supplementary material, which is available to authorized users.

## ACKNOWLEDGMENTS

The authors would like to thank Dr. Yi Jiang and Dr. Edward Hsu for supplying the DTMRI data, as well as Weining Bian for her assistance with the optical profile acquisition of the template wafer. This work

was supported by the American Heart Association Predoctoral Fellowship (No. 0715178U) to Nima Badie.

## REFERENCES

- <sup>1</sup>Badie, N., and N. Bursac. Micropatterned heart slice cultures for studies of intramural cardiac electrophysiology. Paper presented at American Heart Association: Scientific Sessions, Chicago, IL, Nov 15, 2006.
- <sup>2</sup>Badie, N., and N. Bursac. Micropatterned ventricular slice: role of realistic tissue microstructure in impulse conduction. Paper presented at American Heart Association: Scientific Sessions, New Orleans, LA, 2008.
- <sup>3</sup>Badie, N., and N. Bursac. Novel micropatterned cardiac cell cultures with realistic ventricular microstructure. *Biophys. J.* 96(9):3873–3885, 2009.
- <sup>4</sup>Bub, G., K. Tateno, A. Shrier, and L. Glass. Spontaneous initiation and termination of complex rhythms in cardiac cell culture. *J. Cardiovasc. Electrophysiol.* 14(10 Suppl): S229–S236, 2003.
- <sup>5</sup>Bursac, N., F. Aguel, and L. Tung. Multiarm spirals in a two-dimensional cardiac substrate. *Proc. Natl. Acad. Sci. USA* 101(43):15530–15534, 2004.
- <sup>6</sup>Bursac, N., K. K. Parker, S. Iravanian, and L. Tung. Cardiomyocyte cultures with controlled macroscopic anisotropy. A model for functional electrophysiological studies of cardiac muscle. *Circ. Res.* 91:e45–e54, 2002.
- <sup>7</sup>Bursac, N., and L. Tung. Acceleration of functional reentry by rapid pacing in anisotropic cardiac monolayers: formation of multi-wave functional reentries. *Cardiovasc. Res.* 69(2):381–390, 2006.
- <sup>8</sup>Chen, J., S. K. Song, W. Liu, M. McLean, J. S. Allen, J. Tan, S. A. Wickline, and X. Yu. Remodeling of cardiac fiber structure after infarction in rats quantified with diffusion tensor MRI. *Am. J. Physiol. Heart Circ. Physiol.* 285(3):H946–H954, 2003.
- <sup>9</sup>de Diego, C., R. K. Pai, A. S. Dave, A. Lynch, M. Thu, F. Chen, L. H. Xie, J. N. Weiss, and M. Valderrabano. Spatially discordant alternans in cardiomyocyte monolayers. *Am. J. Physiol. Heart Circ. Physiol.* 294(3):H1417–H1425, 2008.
- <sup>10</sup>Entcheva, E., S. N. Lu, R. H. Troppman, V. Sharma, and L. Tung. Contact fluorescence imaging of reentry in monolayers of cultured neonatal rat ventricular myocytes. *J. Cardiovasc. Electrophysiol.* 11(6):665–676, 2000.
- <sup>11</sup>Fast, V. G., and R. E. Ideker. Simultaneous optical mapping of transmembrane potential and intracellular calcium in myocyte cultures. *J. Cardiovasc. Electrophysiol.* 11(5): 547–556, 2000.
- <sup>12</sup>Fast, V. G., and A. G. Kleber. Cardiac tissue geometry as a determinant of unidirectional conduction block: assessment of microscopic excitation spread by optical mapping in patterned cell cultures and in a computer model. *Cardiovasc. Res.* 29(5):697–707, 1995.
- <sup>13</sup>Gao, X., X. He, B. Luo, L. Peng, J. Lin, and Z. Zuo. Angiotensin II increases collagen I expression via transforming growth factor-beta1 and extracellular signal-regulated kinase in cardiac fibroblasts. *Eur. J. Pharmacol.* 606(1–3):115–120, 2009.
- <sup>14</sup>Geerts, L., P. Bovendeerd, K. Nicolay, and T. Arts. Characterization of the normal cardiac myofiber field in goat measured with MR-diffusion tensor imaging. *Am. J. Physiol. Heart Circ. Physiol.* 283(1):H139–H145, 2002.
- <sup>15</sup>Grinnell, F., H. Fukamizu, P. Pawelek, and S. Nakagawa. Collagen processing, crosslinking, and fibril bundle assembly in matrix produced by fibroblasts in long-term cultures supplemented with ascorbic acid. *Exp. Cell Res.* 181(2):483–491, 1989.
- <sup>16</sup>Helm, P., M. F. Beg, M. I. Miller, and R. L. Winslow. Measuring and mapping cardiac fiber and laminar architecture using diffusion tensor MR imaging. *Ann. NY Acad. Sci.* 1047:296–307, 2005.
- <sup>17</sup>Holmes, A. A., D. F. Scollan, and R. L. Winslow. Direct histological validation of diffusion tensor MRI in formaldehyde-fixed myocardium. *Magn. Reson. Med.* 44(1): 157–161, 2000.
- <sup>18</sup>Hooks, D. A., M. L. Trew, B. J. Caldwell, G. B. Sands, I. J. Legrice, and B. H. Smaill. Laminar arrangement of ventricular myocytes influences electrical behavior of the heart. *Circ. Res.*, 2007.
- <sup>19</sup>Hsu, E. W., A. L. Muzikant, S. A. Matulevicius, R. C. Penland, and C. S. Henriquez. Magnetic resonance myocardial fiber-orientation mapping with direct histological correlation. *Am. J. Physiol.* 274(5 Pt 2):H1627–H1634, 1998.
- <sup>20</sup>Iravanian, S., Y. Nabutovsky, C. R. Kong, S. Saha, N. Bursac, and L. Tung. Functional reentry in cultured monolayers of neonatal rat cardiac cells. *Am. J. Physiol. Heart Circ. Physiol.* 285(1):H449–H456, 2003.
- <sup>21</sup>Jiang, Y., K. Pandya, O. Smithies, and E. W. Hsu. Three-dimensional diffusion tensor microscopy of fixed mouse hearts. *Magn. Reson. Med.* 52(3):453–460, 2004.
- <sup>22</sup>Karlon, W. J., J. W. Covell, A. D. McCulloch, J. J. Hunter, and J. H. Omens. Automated measurement of myofiber disarray in transgenic mice with ventricular expression of ras. *Anat. Rec.* 252(4):612–625, 1998.
- <sup>23</sup>Kawara, T., R. Derksen, J. de Groot, R. Coronel, S. Tasserone, A. Linnenbank, R. Hauer, H. Kirkels, M. Janse, and J. de Bakker. Activation delay after premature stimulation in chronically diseased human myocardium relates to the architecture of interstitial fibrosis. *Circulation* 104:3069–3075, 2001.
- <sup>24</sup>Klinger, R., and N. Bursac. Cardiac cell therapy in vitro: reproducible assays for comparing the efficacy of different donor cells. *IEEE Eng. Med. Biol. Mag.* 27(1):72–80, 2008.
- <sup>25</sup>Koura, T., M. Hara, S. Takeuchi, K. Ota, Y. Okada, S. Miyoshi, A. Watanabe, K. Shiraiwa, H. Mitamura, I. Kodama, and S. Ogawa. Anisotropic conduction properties in canine atria analyzed by high-resolution optical mapping: preferential direction of conduction block changes from longitudinal to transverse with increasing age. *Circulation* 105(17):2092–2098, 2002.
- <sup>26</sup>Kucera, J. P., A. G. Kleber, and S. Rohr. Slow conduction in cardiac tissue. II: effects of branching tissue geometry. *Circ. Res.* 83(8):795–805, 1998.
- <sup>27</sup>LeGrice, I. J., B. H. Smaill, L. Z. Chai, S. G. Edgar, J. B. Gavin, and P. J. Hunter. Laminar structure of the heart: ventricular myocyte arrangement and connective tissue architecture in the dog. *Am. J. Physiol.* 269(2 Pt 2):H571–H582, 1995.
- <sup>28</sup>Lijnen, P. J., V. V. Petrov, and R. H. Fagard. Induction of cardiac fibrosis by transforming growth factor-beta(1). *Mol. Genet. Metab.* 71(1–2):418–435, 2000.
- <sup>29</sup>Lim, Z. Y., B. Maskara, F. Aguel, R. Emokpae, Jr., and L. Tung. Spiral wave attachment to millimeter-sized obstacles. *Circulation* 114(20):2113–2121, 2006.

- <sup>30</sup>McSpadden, L. C., R. D. Kirkton, and N. Bursac. Electrotonic loading of anisotropic cardiac monolayers by unexcitable cells depends on connexin type and expression level. *Am. J. Physiol.* 2009.
- <sup>31</sup>Munoz, V., K. R. Grzeda, T. Desplantez, S. V. Pandit, S. Mironov, S. M. Taffet, S. Rohr, A. G. Kleber, and J. Jalife. Adenoviral expression of IKs contributes to wavebreak and fibrillatory conduction in neonatal rat ventricular cardiomyocyte monolayers. *Circ. Res.* 101(5):475–483, 2007.
- <sup>32</sup>Pedrotty, D. M., R. Y. Klinger, N. Badie, S. Hinds, A. Kardashian, and N. Bursac. Structural coupling of cardiomyocytes and noncardiomyocytes: quantitative comparisons using a novel micropatterned cell pair assay. *Am. J. Physiol. Heart Circ. Physiol.* 295(1):H390–H400, 2008.
- <sup>33</sup>Rohmer, D., A. Sitek, and G. T. Gullberg. Reconstruction and visualization of fiber and laminar structure in the normal human heart from ex vivo diffusion tensor magnetic resonance imaging (DTMRI) data. *Invest. Radiol.* 42(11):777–789, 2007.
- <sup>34</sup>Rohr, S., J. P. Kucera, and A. G. Kleber. Slow conduction in cardiac tissue, I: effects of a reduction of excitability versus a reduction of electrical coupling on microconduction. *Circ. Res.* 83(8):781–794, 1998.
- <sup>35</sup>Rohr, S., and B. Salzberg. Characterization of impulse propagation at the microscopic level across geometrically defined expansions of excitable tissue: multiple site optical recording of transmembrane voltage (MSORTV) in patterned growth heart cell cultures. *J. Gen. Physiol.* 104:287–309, 1994.
- <sup>36</sup>Schmid, P., T. Jaermann, P. Boesiger, P. F. Niederer, P. P. Lunkenheimer, C. W. Cryer, and R. H. Anderson. Ventricular myocardial architecture as visualised in post-mortem swine hearts using magnetic resonance diffusion tensor imaging. *Eur. J. Cardiothorac. Surg.* 27(3):468–472, 2005.
- <sup>37</sup>Scollan, D. F., A. Holmes, R. Winslow, and J. Forder. Histological validation of myocardial microstructure obtained from diffusion tensor magnetic resonance imaging. *Am. J. Physiol.* 275(6 Pt 2):H2308–H2318, 1998.
- <sup>38</sup>Scollan, D. F., A. Holmes, J. Zhang, and R. L. Winslow. Reconstruction of cardiac ventricular geometry and fiber orientation using magnetic resonance imaging. *Ann. Biomed. Eng.* 28(8):934–944, 2000.
- <sup>39</sup>Spach, M. S., and J. P. Boineau. Microfibrosis produces electrical load variations due to loss of side-to-side cell connections: a major mechanism of structural heart disease arrhythmias. *Pacing Clin. Electrophysiol.* 20(2 Pt 2):397–413, 1997.
- <sup>40</sup>Spach, M. S., and P. C. Dolber. Relating extracellular potentials and their derivatives to anisotropic propagation at a microscopic level in human cardiac muscle. Evidence for electrical uncoupling of side-to-side fiber connections with increasing age. *Circ. Res.* 58(3):356–371, 1986.
- <sup>41</sup>Valderrabano, M. Influence of anisotropic conduction properties in the propagation of the cardiac action potential. *Prog. Biophys. Mol. Biol.* 94(1–2):144–168, 2007.
- <sup>42</sup>Wu, M. T., W. Y. Tseng, M. Y. Su, C. P. Liu, K. R. Chiou, V. J. Wedeen, T. G. Reese, and C. F. Yang. Diffusion tensor magnetic resonance imaging mapping the fiber architecture remodeling in human myocardium after infarction: correlation with viability and wall motion. *Circulation* 114(10):1036–1045, 2006.